

**Probabilistic Design Space Mapping
Application to Airfoil Design for HAWT**

Mazza, P.; Pereira, R.; De Oliveira, G.

DOI

[10.1088/1742-6596/1618/4/042018](https://doi.org/10.1088/1742-6596/1618/4/042018)

Publication date

2020

Document Version

Final published version

Published in

Journal of Physics: Conference Series

Citation (APA)

Mazza, P., Pereira, R., & De Oliveira, G. (2020). Probabilistic Design Space Mapping: Application to Airfoil Design for HAWT. *Journal of Physics: Conference Series*, 1618(4), Article 042018. <https://doi.org/10.1088/1742-6596/1618/4/042018>

Important note

To cite this publication, please use the final published version (if applicable).
Please check the document version above.

Copyright

Other than for strictly personal use, it is not permitted to download, forward or distribute the text or part of it, without the consent of the author(s) and/or copyright holder(s), unless the work is under an open content license such as Creative Commons.

Takedown policy

Please contact us and provide details if you believe this document breaches copyrights.
We will remove access to the work immediately and investigate your claim.

PAPER • OPEN ACCESS

Probabilistic Design Space Mapping: Application to Airfoil Design for HAWT

To cite this article: P. Mazza *et al* 2020 *J. Phys.: Conf. Ser.* **1618** 042018

View the [article online](#) for updates and enhancements.



IOP | ebooks™

Bringing together innovative digital publishing with leading authors from the global scientific community.

Start exploring the collection—download the first chapter of every title for free.

Probabilistic Design Space Mapping: Application to Airfoil Design for HAWT

P. Mazza¹, R. Pereira² and G. De Oliveira³

Msc Student at TU Delft¹, Assistant Professor at TU Delft and IST Lisbon², Formerly TU Delft, currently Lead Wind Turbine Aerodynamics Engineer at LM Windpower³

E-mail: pmazza017@gmail.com

Abstract. This work presents an airfoil probabilistic design methodology for wind energy applications, using an analytical approach to estimate the angle-of-attack fluctuations produced by non-uniformities in the incoming wind field. The contemplated wind speed perturbations include wind shear, yaw misalignment and atmospheric turbulence, and several combinations of the perturbation sources are considered. A probabilistic design space mapping is carried out to evaluate which wind conditions occur more often in practice and how likely each specific combination of perturbation sources is to occur, for both an onshore and offshore scenario. The proposed probabilistic method and specifically the level of angle-of-attack fluctuations is verified by employing the aero-elastic simulation tool FAST for each case. Finally, the probabilistic approach is used to design airfoils sections employing the genetic multi-objective airfoil optimization tool Optiflow, where the probability of angle of attack fluctuations for a given scenario is used to prescribe the operational angle of attack range over which the airfoil performance is relevant. Results of the airfoil optimization for a 24% thick section are presented, illustrating the trends in foil geometry and aerodynamic performance for three different possible optimization objective functions.

1. Introduction

This work couples a study on the fluctuations of the angle of attack (AoA) experienced by horizontal axis wind turbines (HAWT) with the airfoil design process. It is known that the AoA continuously fluctuates during normal WT operation due to atmospheric perturbations in the wind velocity field and to the structural response of the wind turbine [13]. In the present work an analytical probabilistic approach [1] is employed to evaluate the level of AoA fluctuations at a given blade section for given atmospheric and operational conditions, combined with a probabilistic analysis of how often this conditions occur in practice. Such probabilistic approach has reduced computational costs when considering different scenarios, with respect of numerical analysis tools (e.g FAST). The operational AoA range derived with the probabilistic approach is incorporated into a genetic multi-objective optimization problem, so that it is possible to design airfoils where the performance are optimized over a range of AoA values, where each one is likely to occur. Considering a range of AoA for the airfoil performance is expected to result in more robust airfoil sections. In section 2 the formulation of the probabilistic method is presented and in section 3 several cases are studied to determine how likely different combinations of atmospheric and operational conditions occur in practice. The verification of the method is shown in section 4 and, in section 5, the set up and the results of the airfoil optimization are discussed.



2. Formulation of the Probabilistic Analytical Model for AoA Fluctuations

This section describes the probabilistic analytical model used to estimate the AoA fluctuations which is originally presented in [1]. The analytical model has been derived under the assumptions of steady aerodynamics and infinite blade stiffness. In addition, for simplicity, the pre-cone angle and the tilt angle have been neglected as well as the rotational induction factor. From BEM theory it is known that the inflow angle can be related with the longitudinal and tangential component of the relative velocity as:

$$\phi_0 = \text{atan} \left(\frac{V_{\text{longitudinal},0}}{V_{\text{tangential},0}} \right) \quad (2.1)$$

Where the subscript '0' refers to non-perturbed inflow conditions. In order to account for the wind shear and yaw misalignment effects, the longitudinal and tangential components of the relative wind speed, at a given blade section, can be expressed as:

$$V_{\text{longitudinal},0} = U(h) \cos(\beta) (1 - \bar{a} - K \sin(\psi)) \quad (2.2)$$

$$V_{\text{tangential},0} = \Omega r - U(h) \sin(\beta) \cos(\psi) \quad (2.3)$$

Where β is the yaw angle, \bar{a} is the azimuthally averaged induction factor, ψ is the azimuth angle. In particular $\psi = 0$ when the blade is at the 12 o'clock position. The terms $\sin(\beta)$ and $\cos(\beta)$ are used to describe the geometric effect of yaw misalignment (namely advancing and retreating effect) while the term K is used to account for the skewed wake effect. In addition, the wind shear effect has been accounted for by employing the logarithmic law and considering the hub height h_0 as reference height, where

$$U(h) = U_\infty \frac{\ln(h_0 + r \cos(\psi)) - \ln(z_0)}{\ln(h_0) - \ln(z_0)} \quad (2.4)$$

Where U_∞ is the far upstream wind speed and z_0 is the terrain roughness. From these equations it follows that the inflow angle can be expressed as:

$$\phi_0 = \text{atan} \left(\frac{\cos\beta(1 - \bar{a} - K \sin\psi)}{\lambda_r - \sin\beta \cos\psi} \right) \quad (2.5)$$

Where λ_r is the local tip speed ratio. The effect of the atmospheric turbulence is modelled by defining a relative velocity perturbation δ , dependent on the turbulence intensity I . The relative perturbation is included in the longitudinal direction only; this assumption is justified by the fact that the contribution of a relative perturbation in the tangential direction, in terms of AoA variation, is small because of the large rotational speed and in addition, the tangential (vertical and lateral) component of turbulence intensity is smaller than the longitudinal component. The longitudinal and tangential components of the relative wind speed can be therefore expressed as:

$$V_{\text{longitudinal}} = V_{\text{longitudinal},0}(1 + \delta); \quad V_{\text{tangential}} = V_{\text{tangential},0} \quad (2.6)$$

It follows that:

$$\phi = \text{atan} \left(\frac{V_{\text{longitudinal}}}{V_{\text{tangential}}} \right) = \text{atan} [(1 + \delta) \tan(\phi_0)] \quad (2.7)$$

By recalling that $AoA = \phi - \theta$ and by assuming that the pitch angle is constant during the perturbation δ , because the time scale of turbulence is much smaller than the time scale of the pitch control, it holds that $AoA = \text{atan}[(1 + \delta) \tan(\phi_0)] - \theta$. By defining the AoA fluctuations as $AoA_\delta = AoA - AoA_0$ the following equations can be written:

$$AoA_\delta = AoA - AoA_0 = atan[(1 + \delta)tan(\phi_0)] - \phi_0 \quad (2.8)$$

The atmospheric boundary layer turbulence can be described by a normal (or Gaussian) probability density function (pdf) [6], where the mean $\mu = 0$ and the standard deviation $\sigma = I$, resulting in:

$$p(\delta) = \frac{1}{\sqrt{2\pi}I} e^{-\frac{1}{2}\left(\frac{\delta}{I}\right)^2} \quad (2.9)$$

The pdf for the AoA fluctuations can be found by writing $\delta = \frac{tan(\phi_0 + AoA_\delta) - tan(\phi_0)}{tan(\phi_0)}$ and by applying a change of variable, as follows:

$$q(AoA_\delta|\psi) = \left| \frac{d\delta}{dAoA_\delta} \right| p(\delta) = \frac{1}{\sqrt{2\pi}I |tan(\phi_0)|} |1 + tan^2(\phi_0 + AoA_\delta)| e^{-\frac{1}{2}\left(\frac{tan(\phi_0 + AoA_\delta) - tan(\phi_0)}{I|tan(\phi_0)|}\right)^2} \quad (2.10)$$

The marginal probability of the AoA fluctuations can be computed by integrating equation (2.10) over an entire revolution. Equation (2.10) appears complicated and it is a function of several parameters: turbulence intensity, surface roughness and yaw angle to describe the relative influence of the perturbation sources, the TSR to account for the specific wind turbine operating conditions and the span-wise fraction. In order to obtain an operational AoA range which accounts for all the possible combinations of the above mention parameters experienced by a given HAWT blade section over its lifetime, a 'probabilistic design space mapping' is carried out.

3. Probabilistic Design Space Mapping

This section aims to evaluate the probability of occurrence of different combinations of perturbation sources in order to derive the operational AoA range for a given blade section over its lifetime. For each case, different TSR, I and β are considered, while z_0 is fixed given an installation site. The tip speed ratio and the turbulence intensity are not independent of each other, since they both depend on the mean wind speed. The joint probability of TSR and TI to occur simultaneously can be obtained by multiplying the conditional probability of turbulence intensity given the mean wind speed by the probability of occurrence of the mean wind speed itself [14]; the final probability is given by multiplying it by the probability of occurrence of yaw misalignment, which has been considered independent of the mean wind speed.

$$w_{case} = p(\beta) \times \sum_{i=U_1}^{U_2} [p(I|U_i) \times p(U_i)] \quad (3.1)$$

Where U_1 and U_2 are the lower and upper wind speed limit for the considered TSR. The probability of occurrence of each perturbation source is based on fitted distribution from field data. In particular, for the Offshore scenario: $p(I|U)$ is based on the log-normal distribution of turbulence intensity from the Offshore 'Vindeby' site [10] and $p(U)$ follows the Weibull of a typical Offshore site. Regarding the Onshore scenario: $p(I|U)$ is based on the log-normal distribution of I from the Near-coastal 'Gedser' sites [10] (since no data could be found for an Onshore site) and $p(U)$ follows the Weibull distribution of a typical Onshore site. Finally, for both scenarios $p(\beta)$ follows the normal distribution from the Onshore site 'Slufterdam-West' [9].

Figures 1a and 1b show the average AoA fluctuations for each case and the probability of occurrence of each case, for an Offshore and an Onshore site respectively. The term average is referred to a $[0 \ 360^\circ]$ azimuthal average of the angle of attack fluctuations which has been subsequently averaged over the blade span. The cases on the x-axis are a combination of TSR,

I , β and z_0 summarized in Table 1 (18 cases have been studied for the Offshore site while 33 for the Onshore one, because the range of possible values of turbulence intensity is larger for an Onshore location [7] [8]). From the figures it can be clearly seen how an increase in turbulence intensity results in an increase in the angle of attack fluctuations, while no significant AoA fluctuations increase is detected when changing the yaw angle (see next section) or terrain roughness, indicating that turbulence plays the major role when all perturbation effects are combined. The influence of the TSR can be noticed by comparing for instance case 9 and 18 of the Offshore scenario, where decreasing the TSR from 7 to 3 results in an increase of the AoA fluctuations of about 1° , due to the larger wind speed. Finally, it can be shown that on average, an Onshore site presents a larger average angle of attack fluctuations than an Offshore site.

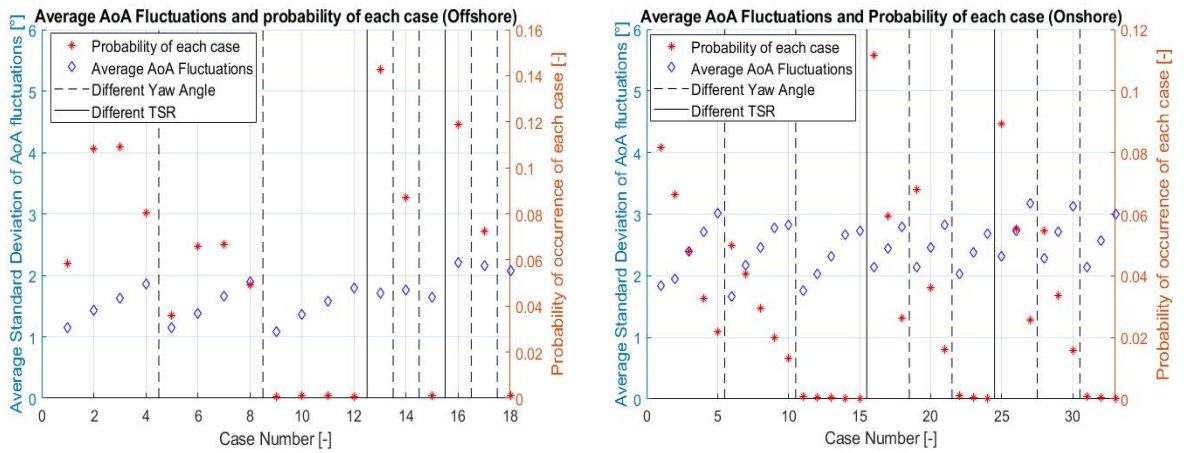


Figure 1: Average (over a revolution and over the blade span) angle of attack fluctuations versus probability of occurrence of each case for an (a) offshore and (b) onshore site. The dashed black lines separate the cases with different yaw angle, while the solid black lines differentiate cases with different TSR.

Referring to Fig 1, the first clear trend can be observed in terms of yaw misalignment angle where the probability of occurrence decreases if the yaw angle increases (e.g. from case 13 to 15, Offshore), reaching values roughly equal to zero for large β (e.g. 20°). It can also be noted that the largest probability of occurrence, for both Offshore and Onshore, is found for $4 < TSR < 6$ and low values of I . This fact can be explained by looking at the conditional probability of turbulence intensity to occur given the wind speed; the mean and standard deviation of the probability density function decrease as the wind speed increases and consequently the probability of occurrence of low I for moderate TSR is large, explaining the peaks in the graph. Moreover, for the Onshore scenario, the probability of occurrence of cases with low values of turbulence intensity is larger than for cases with large I (e.g. from case 1 to 5). This can be explained by pointing out that the conditional probability for I to occur given U is based on a near-coastal site (because no data was found for an Onshore site) where lower values of I are expected.

Once the probability of occurrence of each case is known, it is possible to compute the operational AoA range of an airfoil section by weighting the probability density function of the AoA fluctuations for a given case at a given blade section ($p(\alpha)_{case}$) according to the correspondent weighting coefficient (w_{case}) previously calculated, as follows:

$$p(\alpha)_{total} = \sum_{i=1}^{n_{cases}} p(\alpha)_{case_i} \times w_{case_i} \quad (3.2)$$

Figure 2a and b show the change in the total probability of AoA fluctuations when considering different blade sections and different values of turbulence intensity, respectively. It can be clearly seen how fluctuations decrease moving from inboard towards outboard stations while they increase along with larger I values.

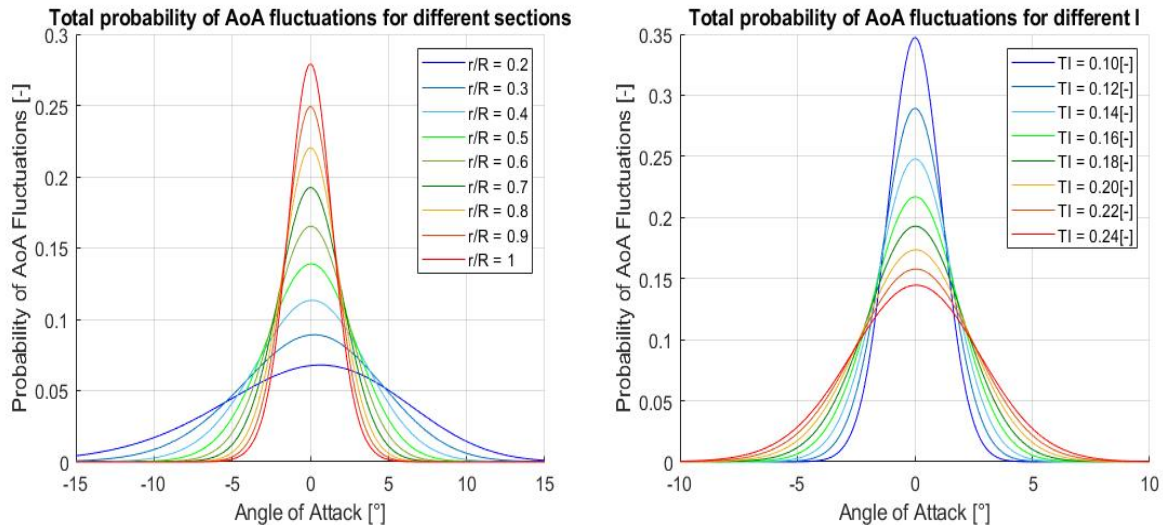


Figure 2: Total probability of AoA fluctuations (a) for different blade sections when $z_0=0.1[m]$, $TSR=7[-]$, $\beta=10^\circ$ and $I = 0.25[-]$ and (b) for different I when $z_0=0.1[m]$, $TSR=7[-]$, $\beta=10^\circ$ and $\frac{r}{R} = 0.50[-]$

Table 1: Summary of the values used for the analysis for each simulated case(*), recalling that the $\frac{r}{R}$ ranges from 0.2 to 1 [-] and z_0 is 0.1 and 0.0002 [m] for Onshore and Offshore, respectively.

*	Onshore	Offshore	*	Onshore	Offshore	*	Onshore
n°	$TSR[-], I[-], \beta[^\circ]$	$TSR[-], I[-], \beta[^\circ]$	n°	$TSR[-], I[-], \beta[^\circ]$	$TSR[-], I[-], \beta[^\circ]$	n°	$TSR[-], I[-], \beta[^\circ]$
1	7, 0.150, 0	7, 0.10, 0	12	7, 0.175, 20	7, 0.16, 20	23	5, 0.140, 20
2	7, 0.175, 0	7, 0.12, 0	13	7, 0.200, 20	5, 0.10, 0	24	5, 0.160, 20
3	7, 0.200, 0	7, 0.14, 0	14	7, 0.225, 20	5, 0.10, 10	25	3, 0.100, 0
4	7, 0.225, 0	7, 0.16, 0	15	7, 0.250, 20	5, 0.10, 20	26	3, 0.120, 0
5	7, 0.250, 0	7, 0.10, 10	16	5, 0.120, 0	3, 0.10, 0	27	3, 0.140, 0
6	7, 0.150, 10	7, 0.12, 10	17	5, 0.140, 0	3, 0.10, 10	28	3, 0.120, 10
7	7, 0.175, 10	7, 0.14, 10	18	5, 0.160, 0	3, 0.10, 20	29	3, 0.140, 10
8	7, 0.200, 10	7, 0.16, 10	19	5, 0.120, 10	-	30	3, 0.160, 10
9	7, 0.225, 10	7, 0.10, 20	20	5, 0.140, 10	-	31	3, 0.120, 20
10	7, 0.250, 10	7, 0.12, 20	21	5, 0.160, 10	-	32	3, 0.140, 20
11	7, 0.150, 20	7, 0.14, 20	22	5, 0.120, 20	-	33	3, 0.160, 20

4. Verification of the Probabilistic Analytical Model

This section aims to verify the modelling of the combined effect of the three perturbation sources. The method is verified by employing the aero-elastic simulator tool FAST, using the 5MW NREL

wind turbine as case study. In order to show a better comparison between the results from the analytical and numerical model, the pre-cone and tilt angle have been set to zero and the tower shadow has been neglected. Each simulation is run according to the values (for an Onshore and Offshore site) summarized in Table 1. The validation of each single perturbation source modelling can be found in [2]. Both the analytical and numerical AoA fluctuations show a decreasing trend over the blade span, which can be explained by the lower rotational speed of inboard stations with respect of outboard stations. This can be observed in Fig 3a and b, where it has been decided to show the best and worst result, which correspond to case 10 and 31 of the Onshore scenario. It should be noticed that the worst result is for a case with large yaw angle and the large difference between numerical and analytical results, at inboard stations, can be attributed to unsteady effects, for instance dynamic stall, which might occur in large yawed conditions [2]. Figures 4a and 4b summarize the results of all the simulated cases and they show the 'smeared' difference between the analytical and numerical results, which is subsequently averaged over the span; referring to the legend, 'total' shows an average of the AoA fluctuations over the span-fraction range [0.2; 1], 'inboard' over [0.2; 0.4] and 'outboard' over [0.4; 1]. It can be seen that overall, the model performs well considering that most of the difference between numerical and analytical results is below 1° and predictions for outboard stations are more accurate than for inboard stations; again, this is because for inboard stations the unsteady effects, which are not accounted for in the analytical model, play a relevant role [15]. Finally, the larger difference between analytical and numerical results is often found for cases with large yaw misalignment angle (20°), indicating that large β do have an impact on the AoA fluctuations, in contrast with what the analytical model predicts. It should also be noticed that few seconds are needed to run a case using the analytical approach while 10-15 minutes to run a case (for 360s) with FAST, resulting in substantial reduction of computational costs. A better accuracy could be achieved in future works by using the AoA time series of the different cases obtained with FAST to assess the probability of occurrence with inclusion of aeroelastic effects, as well as rotationally sampled turbulence spectra; of course, losing the advantage of the analytical approach, since an aeroelastic tool would be required. For the present study the goal is to illustrate the impact of the analytical probabilistic approach in the design process.

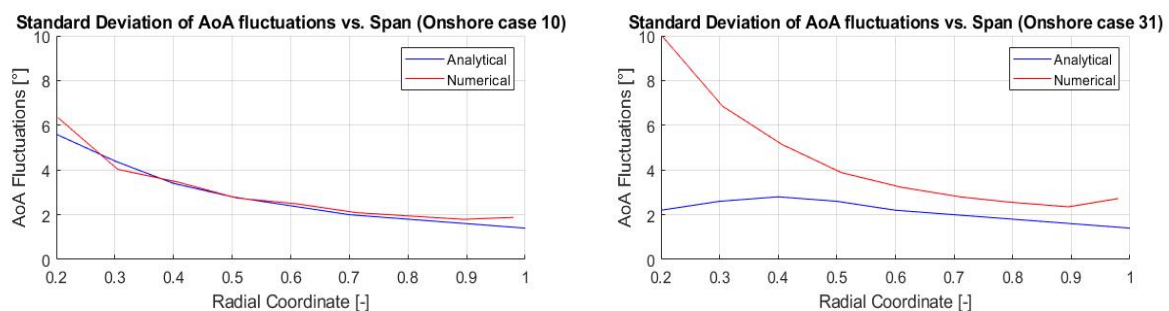


Figure 3: Standard deviation of the AoA fluctuations for (a) the Onshore site case 10 ($TSR=7[-]$, $I=0.25[-]$, $\beta=10^\circ$) and $z_0=0.1[m]$) and (b) for the Onshore site case 31 ($TSR=3[-]$, $I=0.12[-]$, $\beta=20^\circ$) and $z_0=0.1[m]$)

5. Airfoil Design and Optimization

5.1. Optimization Set-up

This section briefly summarizes the set-up of the optimization. The optimization has been performed by using the genetic multi-objective optimization tool: Optiflow [4]. 50 generations have been considered, where each generation includes an airfoil population of 150 individuals. The main convergence criteria is based on the sparsity along the Pareto Front which is accounted

for by imposing a Pareto fraction of 60 %. In addition, Optiflow uses the CST parametrization described in [4], which employs the 8th order of the Bernstein polynomials (for both the upper and lower surface) to parametrize the airfoil geometry. The aerodynamic performance (i.e polar curves) are calculated by using RFOIL and assuming a Reynold's number of 9×10^6 , which is typical for large horizontal axis wind turbines [11]. RFOIL predicts transition based on the e^n method [12] and the critical amplification factor n has been set to 9. The clean configuration corresponds to free transition whereas the rough configuration has been evaluated by fixing a transition location on the upper and lower surface of $\frac{x}{c} = 0.05$ $\frac{x}{c} = 0.1$, respectively [3]. Finally, each polar curve has been calculated for an AoA ranging from -5° to 20° in steps of 0.2° .

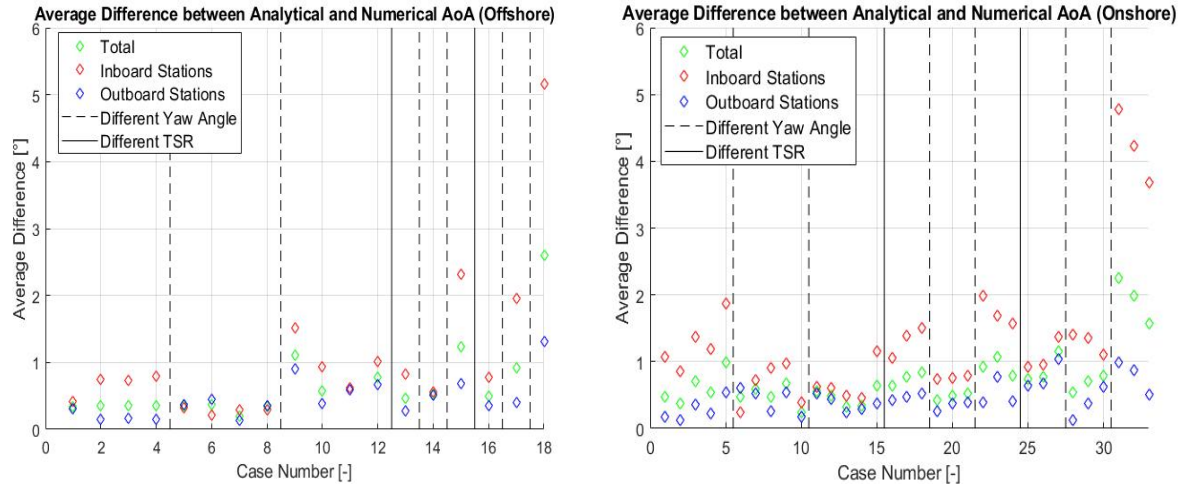


Figure 4: Overview of the 'smeared' difference between the numerical and analytical results for each case of (a) an Offshore and (b) an Onshore site. The dashed black lines separate the cases with different yaw angle, while the solid black lines differentiate cases with different TSR.

Table 2: Summary of the CFs used for the airfoil optimization, where MF stands for mingle factor equal to 0.5 and C_l in $CF_{3.1}$ is evaluated in the clean configuration. The minus sign in the CFs is for ease of objective within the optimization framework

- Cost Function	
$CF_{1.1}$	$-\frac{C_l(\alpha_{opt})}{C_d(\alpha_{opt})}\Big _{clean}$
$CF_{1.2}$	$-\int_{\alpha_{opt}-\sigma_{alpha}}^{\alpha_{opt}+\sigma_{alpha}} \frac{C_l(\alpha)}{C_d(\alpha)}\Big _{rough} \times p(\alpha) d\alpha$
$CF_{2.1}$	$-\left[(1 - MF) \frac{C_l(\alpha_{opt})}{C_d(\alpha_{opt})}\Big _{clean} + MF \frac{C_l(\alpha_{opt})}{C_d(\alpha_{opt})}\Big _{rough} \right]$
$CF_{2.2}$	$-\left[(1 - MF) \int_{\alpha_{opt}-\sigma_{alpha}}^{\alpha_{opt}+\sigma_{alpha}} \frac{C_l(\alpha)}{C_d(\alpha)}\Big _{clean} \times p(\alpha) d\alpha + MF \int_{\alpha_{opt}-\sigma_{alpha}}^{\alpha_{opt}+\sigma_{alpha}} \frac{C_l(\alpha)}{C_d(\alpha)}\Big _{rough} \times p(\alpha) d\alpha \right]$
$CF_{3.1}$	$\left C_l(\alpha_{opt} + \sigma_{alpha}) - C_l(\alpha_{opt} - \sigma_{alpha}) \right + \left C_l(\alpha_{opt}) - C_l(\alpha_{opt} - \sigma_{alpha}) \right $
$CF_{3.2}$	$CF_{2.2}$

Table 3: Summary of the constraints used for the airfoil optimization. Where pf stands for penalization factor and pf_{90} are respectively the thickness exceedance at $\frac{x}{c} = 75\%$ and $\frac{x}{c} = 90\%$.

Type	Aerodynamic Constraints
Upper bound	$\frac{L}{D}(\alpha_{opt}) _{clean} < 300$; $\frac{L}{D}(\alpha_{opt}) _{rough} < 160$
Lower bound	$\alpha_{opt} > 0$; $C_l(\alpha_{opt}) > 0.6$
Type	Geometric Constraints
Minimum TE Thickness	$pf_{minthickness} = (1 - pf_{75})^2 \times (1 - pf_{90})^2$
Negative Concavity (suction side)	$\frac{\partial^2 t}{\partial x^2} < 0$

5.2. Cost Functions Definition and Constraints

This section discusses the cost functions (CF) and the constraints used in the optimization, which are listed in Table 2 and 3. Several arguments are usually considered when designing airfoils, among which the most relevant are large C_l and high lift-to-drag ratio to increase aerodynamic efficiency, large margin between optimal and stall AoA to try to avoid off-design conditions [5] and insensitivity to roughness so that the airfoil performance are not sensitive to leading edge degradation, due to soiling impurities and erosion [3]. Another possible requirement could be aiming at load reduction, by limiting the C_l variation over the operational AoA range; a fairly flat C_l polar reduces the sensitivity of C_l to the AoA fluctuations, reducing fatigue. The present work mainly aims to evaluate the impact of the probabilistic approach with respect of a point-design strategy on the airfoil design and to do so, the CFs optimize the $\frac{L}{D}$ both at the optimal AoA and over the operational AoA range previously calculated. The roughness insensitivity considerations are accounted for by evaluating the airfoil polars in clean and rough configuration, while the large margin between AoA_{opt} and AoA_{stall} is partially included by weighting the $\frac{L}{D}$ over the operational AoA range, since, if the stall AoA is close to the optimal AoA, the lift coefficient will decrease within the AoA range and so the $\frac{L}{D}$. The aerodynamic constraints have been set to exclude ultra-high or ultra-low performance, by ensuring a positive optimal AoA and a $C_{l_{opt}} > 0.6$ while the lift-to-drag ratio, in clean and rough configuration, is limited within realistic values. The geometric constraints ensure that the airfoil is feasible under the manufactural point of view by imposing a minimum TE thickness based on the thickness exceedance with respect of the reference airfoils used in 5MW NREL turbine and that the upper surface concavity is always negative, this is because a change in concavity might increase the adverse pressure gradient [11].

5.3. Optiflow Results for a 24% thick airfoil

This section discusses the Optiflow results for a 24% thick airfoil for three different cases, namely (1) evaluating the $\frac{L}{D}$ at the optimal AoA in the clean configuration ($CF_{1.1}$) and weighting the $\frac{L}{D}$ across the operational AoA range in the rough configuration ($CF_{1.2}$); (2) evaluating the $\frac{L}{D}$ at the optimal AoA including both clean and rough configuration ($CF_{2.1}$) and weighting the $\frac{L}{D}$ across the operational AoA range for both the clean and rough configuration ($CF_{2.2}$); (3) aiming at load reduction in the operational AoA range ($CF_{3.1}$) and same as ($CF_{2.2}$).

Figure 5 shows the results of case 1. For the sake of clarity only three airfoils from the complete Pareto front are presented, corresponding to largest value of $CF_{1.1}$ (blue), largest value of $CF_{1.2}$ (red) and 50-50 compromise between $CF_{1.1}$ and $CF_{1.2}$ (green). Regarding the airfoil

geometry it can be observed that moving from blue to red the maximum thickness moves towards lower $\frac{x}{c}$ and the camber decreases, which directly results in a shift of the lift polar. In addition, the three airfoils present an s-shaped lower surface which is desirable in order to generate more Lift, by increasing the aft-loading [3]. By comparing the lift polars in the clean and rough configuration, it can be noticed that roughness insensitivity increases moving from blue to red. This result makes sense because the red airfoil maximizes the $\frac{L}{D}$ in the rough configuration, and it also shows that a possible way to reduce roughness sensitivity is to adopt airfoils with low maximum upper thickness. However, the red airfoil shows a large optimal AoA (around 14°) which is not desired for WT application since, when operating at low AoA, separation might occur on the pressure side and moreover, the C_l values at low AoA are very poor.

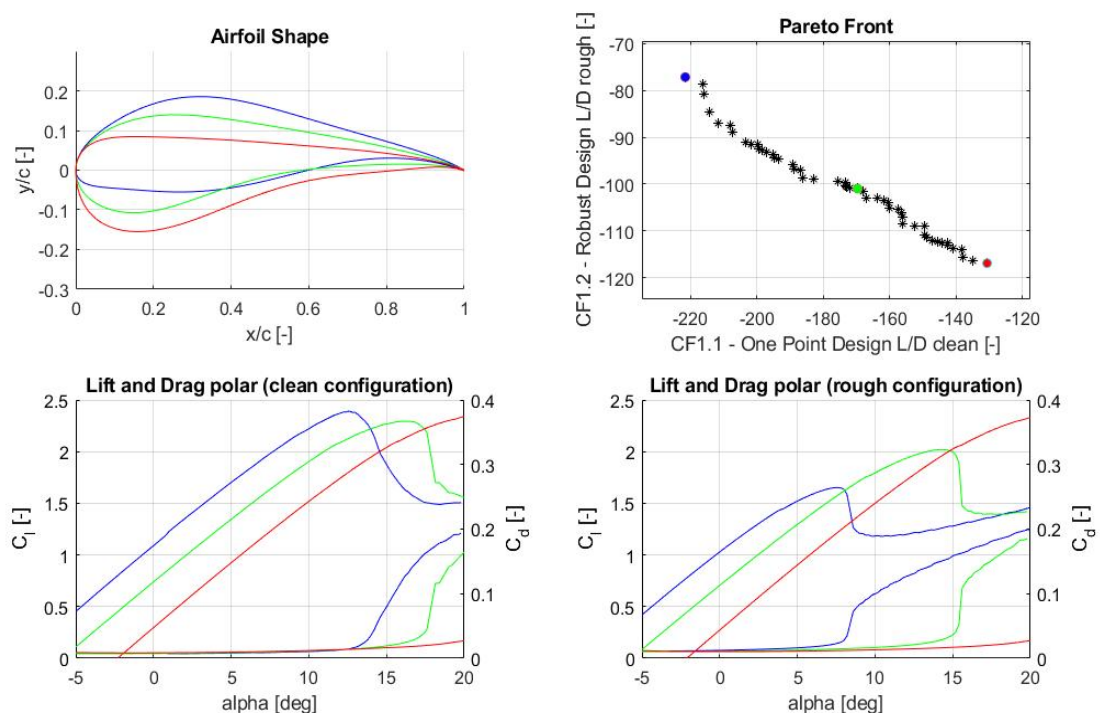


Figure 5: (a) Airfoil shapes and (b) correspondent polar curves for a 24 % thick airfoil. The blue line correspond to the airfoil with largest value of $CF_{1,1}$, the red lines to an airfoil with largest values of $CF_{1,2}$ and the green lines to a 50-50 compromise between $CF_{1,1}$ and $CF_{1,2}$.

Figure 6 illustrates the results of case 2. The first thing that should be noticed is the very small airfoil geometry variation along the Pareto front. This should be due to the choice of trading off between the $\frac{L}{D}$ in clean and rough configuration, which decreases the difference between the two CFs, resulting in comparable outcomes. Regarding the airfoil geometry, the airfoils present a lower s-shaped surface and a sharp LE nose. The latter characteristics might promote an earlier transition which may delay flow separation. Besides, with respect of the previous case, the maximum thickness is shifted downstream. The combination of these features leads to a very balanced airfoil in terms of aerodynamic characteristics, since large values of C_l along with a good roughness insensitivity and large margin between the optimal and stall AoA (around 7° and 5° for the clean and rough configuration, respectively) are achieved. This airfoil has been compared with the reference DU91W2-250 airfoil, as can be seen in Fig 7. The two airfoils presents a

very similar shape; the novel designed airfoil has a larger camber and a larger maximum upper thickness than the DU airfoil. These characteristics lead to larger Lift produced, which makes sense since the objective of the optimization was maximizing $\frac{L}{D}$, but the lower maximum upper thickness of the DU airfoil is probably the reason for the best roughness insensitivity achieved by the DU airfoil.

Figure 8 shows the results of case 3. It can be seen how the load reduction goal is achieved for the blue airfoil, which shows a fairly flat lift polar for $AoA > AoA_{opt}$. The blue airfoil presents the unique geometric feature of thick TE along with a 'w-shaped' lower surface. These characteristics should imply that the flow is accelerated in two steps first by the LE and subsequently from around $\frac{x}{c} = 0.5$ to $\frac{x}{c} = 0.8$; this flow 'modulation' might justify the fairly flat lift polar.

Generally speaking, the presented airfoils show really high C_l values, being the lift-to-drag ratio at the core of the optimization, and among them the result of case 2 is probably the best outcome for wind turbine applications. The main goal of this section was to explore the potential of the analytical approach and to show its applicability for airfoil design. In this regard, more elaborate CFs should be used when designing airfoils for real purposes.

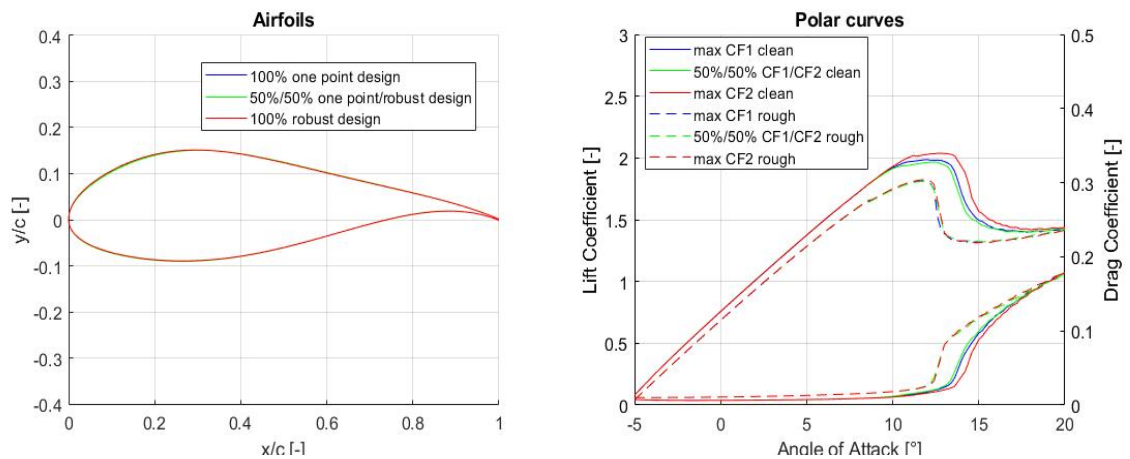


Figure 6: Simulation result for a 24 % thick airfoil at 50 % of the span, where $CF1 = CF_{2.1}$ and $CF2 = CF_{2.2}$. a) airfoil geometry, b) polar curves in the clean and rough configuration

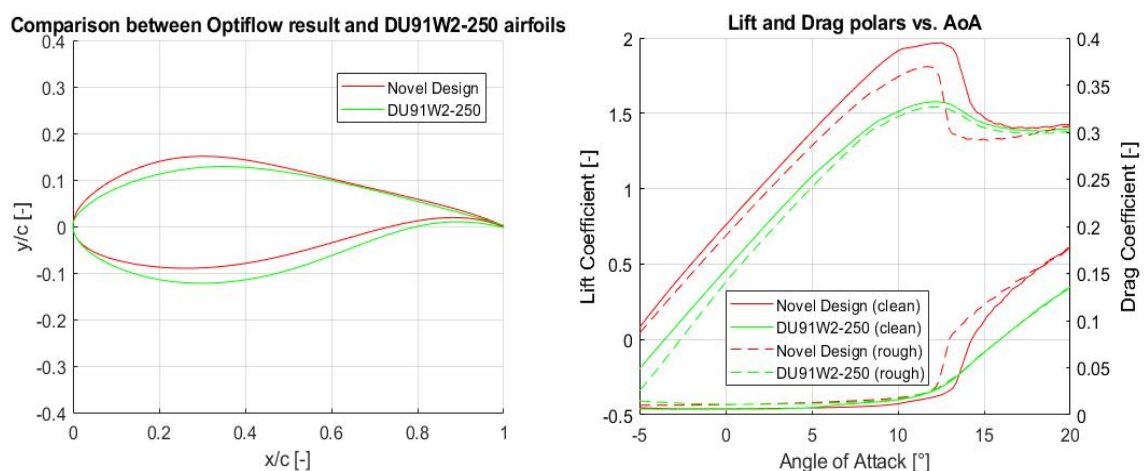


Figure 7: Comparison between the Novel Designed airfoil (case 2) and the reference DU91W2-250 airfoil. a) airfoil geometry, b) polar curves in the clean and rough configuration

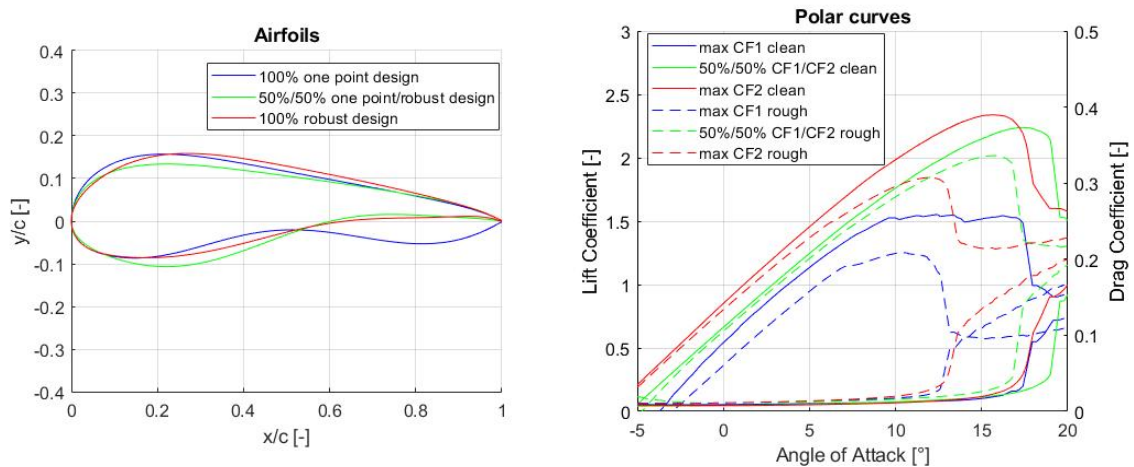


Figure 8: *Simulation result for a 24 % thick airfoil at 50 % of the span, where $CF1 = CF_{3.1}$ and $CF2 = CF_{3.2}$. a) airfoil geometry, b) polar curves in the clean and rough configuration*

6. Conclusions

This work describes the probabilistic approach for designing airfoils for WE applications. The probabilistic approach derives an expression to estimate the fluctuations of the AoA according to the atmospheric perturbations in the relative velocity seen by the airfoil. The probabilistic design space mapping shows that atmospheric turbulence has the largest effect in terms of resultant AoA fluctuations and it presents an expression to estimate the probability of occurrence of given combination of atmospheric perturbations. A verification has been carried out to evaluate the accuracy of the probabilistic method predictions for several cases and for two different installation sites (Onshore and Offshore). It has been showed an average difference (definition of average in section 4), between the analytical (probabilistic approach) and numerical (FAST) results generally lower than 1° . The larger difference between numerical and analytical results is found for cases with large yaw angle (e.g. 20°); however, the probability of occurrence of such cases is very small, which limits the impact of this error. The probabilistic approach has been used to optimize airfoils, in particular, for a 24% thick airfoil using three different CFs. The resultant foil geometry is generally similar to reference WE airfoils, particularly retaining the somewhat shape nose and S-shaped lower surface. The aerodynamic performance of the newly designed airfoil sections is also compliant with typical WE requirements, namely displaying large lift-to-drag ratio, a relatively large margin between optimal and stall AoA and also roughness insensitivity. These results indicate the probabilistic approach is a valid methodology to enhance the robustness of the airfoil design process and may be used to obtain airfoil sections tailored for specific WE applications and operational conditions.

References

- [1] R. Pereira et al, 2018, IOP Conf. Series: Journal of Physics 1037 (2018) 022042, 'Probabilistic Design of Airfoil for Horizontal Axis Wind Turbines';
- [2] P.Mazza, 2020, Master Thesis of Science, TU Delft, 'Probabilistic Design of Airfoils for Horizontal Axis Wind Turbine';
- [3] R.P.J.O.M. van Rooij, W.A. Timmer, 2003, AIAA 2003-50, 41st Aerospace Sciences Meeting and Exhibit, 'Roughness Sensitivity Considerations for Thick Rotor Blade Airfoils';
- [4] G. de Oliveira, 2011, TU Delft Master Thesis, 'Wind Turbine Airfoils with Boundary Layer Suction: A Novel Design Approach';

- [5] F. Grasso, 2011, Journal of Aircraft, Vol 48 no 1, 'Usage of Numerical Optimization in Wind Turbine Airfoil Design', DOI: 10.2514/1.C031089;
- [6] D. Veldkamp, 2006, DUWIND, 'Chances in Wind Energy: A Probabilistic Approach to Wind Turbine Fatigue Design', ISBN-13:978-90-76468-12-9;
- [7] IEC 61400-1:2005(E), INTERNATIONAL STANDARDS, 2005, 'Wind Turbine - Part 1: Design Requirements';
- [8] IEC 61400-3:2009-02, INTERNATIONAL STANDARDS, 2009, 'Wind Turbine - Part 3: Design Requirements for Offshore Wind Turbines';
- [9] S. Goossens, 2015, Master Thesis of Science, TU Delft, 'Field-Test of Nacelle-based Lidar to explore its applications for Vattenfal as Wind Park Operator';
- [10] G.C. Larsen, 2001, WIND ENERGY, 4:107-120, 'Offshore Fatigue Design Turbulence', DOI:10.1002/we.49;
- [11] R. Pereira, 2016, TU Delft Phd Thesis, 'Active Stall Control of Horizontal Axis Wind Turbine: A Dedicated Study with Emphasis on DBD Plasma Actuators', ISBN 978-94-6299-417-1;
- [12] J. L. van Ingen, 2008, AIAA 2008-3830, 38th Fluid Dynamic Conference and Exhibit, 'The e^n method for transition prediction: Historical review of work at TU Delft';
- [13] G.J. Leishman, G.L. Martin, 2002, Wind Energy 5:85-132, 'Challenges in Modelling the Unsteady Aerodynamics of Wind Turbines', DOI: 10.1002/we.62;
- [14] R. B. Ash, 2008, DOVER PUBLICATIONS, INC. 'Basic Probability Theory';
- [15] H. Snel, 2004, Conference Proceedings European Wind Energy Conference, ECN-RX-04-120, 'Application of Modified Theodorsen model to the estimation of Aerodynamic Forces and Aeroelastic Stability'.